Scanning illumination-acquisition system for noncontact optical tomography

Ignacio Iglesias
Universidad de Murcia
Departamento de Física
Campus de Espinardo
30100 Murcia, Spain

Jorge Ripoll
Institute of Electronic Structure & Laser (IELS)
Foundation of Research & Technology Hellas (FORTH)
Vassilika Vouton
71110 Heraklion, Crete
Greece

Abstract. A new method for the detection of light traversing a diffuser/nondiffuser interface and its simultaneous determination for optical tomography is proposed, and the preliminary results are shown. The method is based on the use of a point detector and two uncoupled scanning systems—one for illumination and the other for registration—together with active modification of the optics guided by the surface topography to generate virtual detectors on the interface.
 [DOI: 10.1117/1.3103290]

Keywords: tomography; fluorescence; active optics; adaptive optics; multiple scattering; medical imaging.

Paper 08313R received Sep. 9, 2008; revised manuscript received Dec. 31, 2008; accepted for publication Jan. 2, 2009; published online Mar. 23, 2009.

1 Introduction

Optical tomography is a noninvasive technique that uses light to obtain spatially resolved information of biological states or processes within tissues, even *in vivo*, in a high scattering and absorption propagation regime. In its fluorescence modality, the technique is able to track the concentration and trafficking of molecules using functionalized fluorescence markers.[1] Unlike other probes, light is reflected and deviates, changing its intensity when it passes through interfaces separating regions with different optical properties. This means that, apart from the data provided by the intensity of the light traversing the surface, information on its tridimensional geometry is also required for reconstruction algorithms.

Traditionally, optical fibers with apertures placed in contact with the surface have been used to generate illumination sources—excitation sources in fluorescence tomography modality—and detectors on the surface, when coupled with lasers or with sensors. This solution has several drawbacks, including limited sampling and a complex and unstable setup. Furthermore, despite the fact that the surface itself is used for the coupling, its position in space remains undetermined, so additional instrumentation is necessary to measure the topography.

In optical fluorescence tomography, recently proposed noncontact schemes[2–5] have avoided the use of optical fibers in the detection process. Instead, these methods use CCD cameras and take into account the free-space propagation of light from the surface to the sensor. In the first implementations, optical fibers were still used as the excitation mechanism but were later replaced[6–9] by laser beams with scanning mirrors as free-space light delivery mechanism to the sample.

Although the need for optical fibers was removed, independent determination of the surface was still needed. For this, several methods have been applied, such as structured light photogrametry[3] or surface determination from projection.[4] Whichever is used, additional instrumentation is necessary, although this introduces complexity into the setup and possible sources of error due to the potential incorrect matching between the real position of the detectors in space and the position derived from the surface data.

In this work, we propose a new approach based on active optics that involves using a double uncoupled scanning system. In order to generate illumination sources on the surface, the first scanning system generates an excitation spot on the boundary; simultaneously, the light emerging from an area generally centered at a different position on the surface is conducted by a second scanning system and measured using a photodetector with a point aperture. To account for the different depths related with the different surface positions, the optical system actively changes by adjusting the focus.

Apart from the sensitivity gained by using a photodetector and its compactness, the main advantage of this new acquisition scheme over previous noncontact systems is that the data are obtained on the interface surface by optical conjugation with a point detector aperture, in a manner akin to the optical fiber solution but without its drawbacks. Unlike in CCD systems, the data set recorded in this way is ready to be used in the tomographic reconstruction algorithms and, since the need to numerically propagate the sensor data disappears, it is free of matching errors and consequently able to offer superior results.

Based on this general idea, different strategies can be followed to modify the optics and to obtain the data necessary to drive it. The most direct approach is presented here in the form of a preliminary demonstration of an acquisition system for use in fluorescence tomography, where the change in the optical system is accomplished by moving a lens on a translation stage for each detector point with displacements obtained by using the depth-resolving property of the confocal system.[10]

Details of the experimental system, its optical characteristics, and its basic operation are demonstrated using a schematic solid phantom of known simple fluorochrome distribution.

Address all correspondence to: Ignacio Iglesias, Departamentode de Física, Universidad de Murcia, Campus de Espinardo, 30100 Murcia, Spain. E-mail: iic@um.es.

1083-3668/2009/14(2)/024003/7/$25.00 © 2009 SPIE

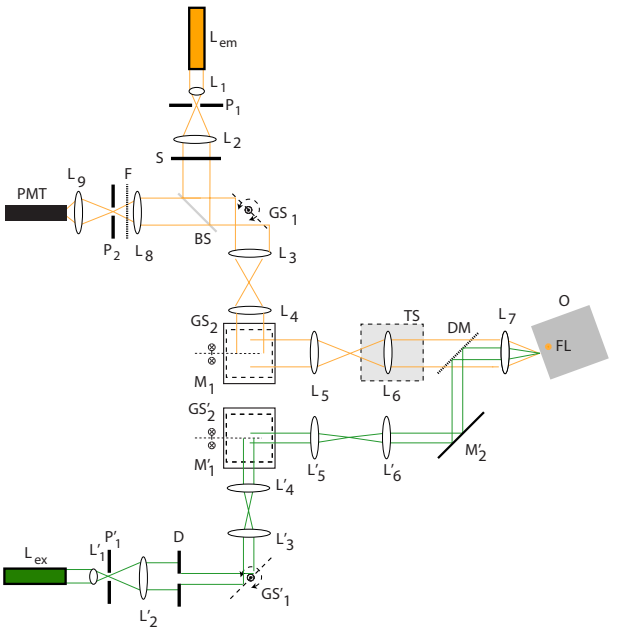

Fig. 1 Schematic drawing of the noncontact optical fluorescence tomography system.

2 Materials and Methods

2.1 *Experimental System*

The system is depicted in Fig. 1. A diode-pumped solid-state green laser with a 532-nm wavelength (Laser Quantum) is used as the fluorochrome excitation source, L_{ex}. The laser beam is spatially filtered and collimated using lenses, L'_1 and L'_2, the pinhole, P'_1, and the diaphragm, D, to form a relatively thin beam (1.5-mm diameter, approximately). A pair of galvanometric scanners (GSI Lumonics, VM500), GS'_1 and GS'_2 (broken line), are placed in conjugate planes, which are also conjugated with the plane where the lens L_7 is placed, using for this purpose lenses L'_3 to L'_6. The rotation axes of GS'_1 and GS'_2 are perpendicular and parallel, respectively, to the drawing plane of Fig. 1. In this configuration, when voltages are applied, the mirrors rotate, causing the beam to pivot around the optical axis at the plane of L_7 ($f=100$ mm), generating an excitation source of approximately 50 μm diameter (assuming an Airy spot) in different positions on the surface of the object, O, with embedded fluorochrome distribution, FL. In Fig. 1, the beam is also conducted using the standard mirrors M'_1 and M'_2 and the dichroic mirror DM (z532rdc from Chroma) which allows 1% of the green light reflected back by the object surface to pass through it. An additional orange He–Ne laser, L_{em}, 594-nm wavelength (Thorlabs), is spatially filtered and collimated to generate a beam that, contrary to the excitation laser, uses the maximum aperture allowed by the optical components. This beam passes through an electromechanical shutter, S, and through a pellicle reflection beamsplitter, BS (92% transmission–8% reflection). The light is then reflected by two additional galvanometric mirrors, GS_1 and GS_2, in the same configuration described earlier, and passes with no significant absorption through the dichroic mirror, DM, and lens L_7 to reach the object surface.

The lens L_6 is placed on a motorized translation stage, TS (Micos, PLS-85), to control the focus of the orange beam at a given point on the interface. The diffused light reflected from the surface forms an emission point source, whose light follows the reverse path to reach the sensor, a photomultiplier tube, PMT (Electron Tubes, 9129B). In front of the sensor aperture, the lens L_8 conjugates—at the translation stage in-focus position—a 200-μm-diam pinhole, P_2, with the surface. A filter, F (Chroma, HQ580/60m), is placed before the sensor with a passband of between 545 nm and 615 nm, which completely blocks the green laser. Taking into account the magnification of the optical system, P_2 scales to 170 μm diameter on the surface.

2.2 *Acquisition Procedure*

The voltage generated by the PMT was acquired using a high-speed (100 Ms/s) 8-bit resolution digitizer board (National Instruments, NI5112), and the control software was written in LabView, splitting the operation into two phases. First, two voltages are applied to the mirrors (GS_1 and GS_2) according to a specific transversal point with coordinates (y,z); then, a transistor-transistor logic (TTL) signal is sent to open the shutter, S, and a relatively high voltage is sent to the mirror GS'_1 thus deviating the excitation beam out of the path. In this state, the surface becomes illuminated only with light from the laser L_{em}, and there is no fluorescence emission. In this configuration, the translation stage moves to find the displacement that maximizes the sensor signal. This position, which is directly related to a particular surface depth (x coordinate), brings the pinhole P_2 into focus with the surface by placing a virtual detector at the vector position $\vec{r}_i=(x,y,z)$ on the surface. In the second phase, the translation stage is maintained in the previously found position, the shutter S closes, and registration of the fluorescence signal from the PMT begins for the different voltages applied on the mirrors GS'_1 and GS'_2 associated to the excitation source vector $\vec{r}_k$. This provides the data set, $J(\vec{r}_i,\vec{r}_k)$, which is suitable for tomographic reconstruction.[3] Unlike in the acquisition subsystem, where the maximum allowed apertures are used to obtain information on maximum wave vector diversity, it is assumed that the beam diameter of the excitation laser is small enough to be always in focus on the surface, the x coordinate obtained in the first phase serving to completely specify the $\vec{r}_k$ vector.

Although the previous procedure is suitable for obtaining a complete data set, the following results are obtained for dense registration using a small number of excitation positions. For this purpose, the software allows the process to be reversed: with S open, a high voltage is applied to GS'_1 to prevent fluorochrome excitation, and the voltages associated to the $\vec{r}_i$ detector position are sent to the mirrors GS_1 and GS_2, initiating the focus search. Once concluded, two voltages are sent to the mirrors GS'_1 and GS'_2 to generate an excitation source at $\vec{r}_k$, and the intensity of the fluorescent light is measured.

2.3 *Calibration*

To test the system's performance in terms of field of view, resolution, and range of focus that can be controlled, conventional intensity images of a chart were registered. For this, a flat squared regular mesh, obtained by printing black lines on

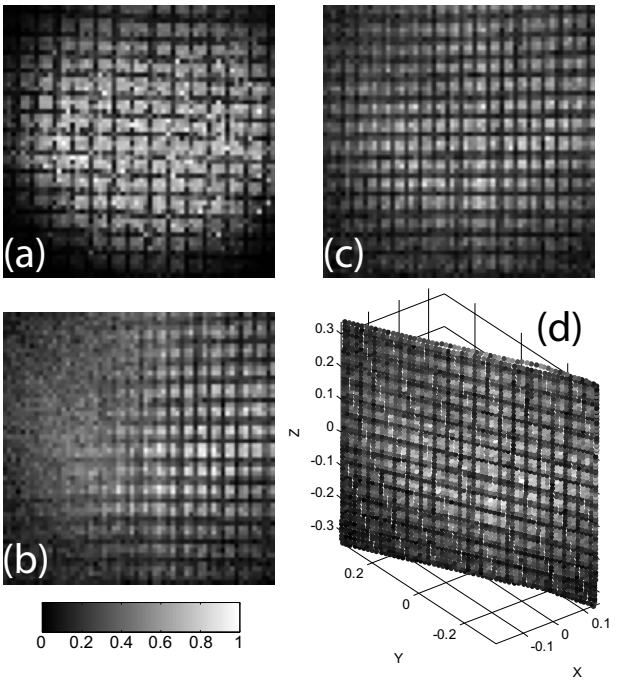

Fig. 2 (a) Image acquired with the calibration test placed perpendicular to the optical axis. (b) Image obtained with the test tilted. (c) Image obtained with the test tilted and the translation stage moving. (d) The same intensity values as in (c) represented in three dimensions using the obtained surface information. The images have 60×60 pixels, the units are millimeters, and the intensity has been normalized.

white paper with 0.5-mm pitch, was used and, to obtain images of the reflected light, a yellow LED was used to illuminate the target. Part of the LED spectrum was able to pass through the dichroic mirror and the filter, and so no modification of the optical system was needed, apart from including in the control the capability of switching the LED on and off when the shutter S is closed or opened. Given that the surface is flat, to speed the process, a low-resolution image of 20×20 points was first acquired and the surface information obtained was used to drive the translation stage for finer acquisitions.

Figure 2(a) shows the image obtained when the test is oriented perpendicular to the optical axis and the translation stage is fixed at the distance corresponding to the pixel on the optical axis. In this situation, the system is similar to a conventional digital camera, where the pinhole acts as a sensor element and the number of samples and the detector spacing are controllable by the voltages, while the field of view and the magnification depend on the maximum voltage and focal length of L_7. With the available optics, we can use a maximum range of ± 0.4 V, producing a field of view of 0.668 cm. Although the illumination of the object was not even, the circular fading that can be seen in Fig. 1(a) is caused not by the illumination intensity distribution but by the limited apertures of the lenses between the galvanometric mirrors. Figure 2(b) shows the smearing of areas that become out of focus when the test is tilted. Figure 2(c) shows the image obtained when adapting the focus by moving the translation stage for each pixel. Panel (d) shows the same intensity values as in Fig. 2(c), rendered as gray scaled dots placed in space in accordance with the encoded surface data. With the current optical system, we obtained a 0.3-cm adjustable depth range. Figure 2(c) also shows a distortion in the image of the test due to a slight nonlinearity between the voltages applied to the mirrors and the transversal position coordinates.

Note that the described focusing method results in variable acquisition numerical aperture and a disparity (depending on the axial coordinate) between the expected lateral surface coordinates addressed by the voltages and the real coordinates for the measured intensity for off-axis points. These two effects could induce artifacts in a tomographic reconstruction algorithm if the register data set is not modified accordingly before use. However, in the current system, they are not significant given the long focal length of L_7 compared with the depth variation and the field of view.

2.4 *Phantom*

To test the system with fluorescence in a simulated biological medium, a solid cylindrical phantom,[11] shown in the central inset of Fig. 3, was fabricated. Isophthalic polyester resin and catalyst were mixed with India ink and titanium dioxide nanopowder (Sigma-Aldrich) before curing in adequate quantities to simulate scattering and absorption of approximately $\mu_s' = 8\ \mathrm{cm}^1$ and $\mu_a = 1.4\ \mathrm{cm}^1$. To better evaluate the performance without restricting the generality of the method, instead of using a complicated surface, one of the flat surfaces of the phantom was used as simulated air/tissue interface.

A cylindrical hollow—also shown on the central inset of Fig. 3—of 1 mm diameter was drilled centered approximately 1.5 mm from the interface surface and filled with a water solution of Alexa A538 (Invitrogen) in the form of goat anti-mouse IgG (H+L) with a concentration of 0.2 mg/ml.

A548 fluorochrome was chosen to demonstrate the operation of the system using the lasers and sensor available in the laboratory. The 532-nm laser is able to excite the fluorescence with a quantum efficiency of around 40%, obtaining emission at 603 nm, close to the He-Ne laser orange wavelength. The dichroic mirror and filter combination is suitable for these excitation/fluorescence wavelengths and also allows the He-Ne laser light to pass through them.

3 Fluorescence Measurements

3.1 *Acquired Data in an Unbounded Infinite Medium*

The first experiment consisted of registering images of the phantom surface with fluorescence light for several excitation points. The data was obtained acquiring 0.5 Ms of the *PMT* output voltage. Given that the scanners have a limited bandwidth of around 3 kHz, the preceding parameter determines the total acquisition time. We limited the sampling to 60×60 pixels and ± 0.2 V voltage range for the mirrors GS_1 and GS_2 corresponding to a window of 3.34 mm $\times$ 3.34 mm. This area is represented as the shaded square in the central inset of Fig. 3.

In a first experiment, the phantom was placed with its flat surface closest to the fluorochrome column and perpendicular to the excitation beam that follows the direction of the arrow shown in Fig. 3(a) [zero voltage applied to mirrors GS_1' and GS_2' or $\vec{r}_{exc} = (0,0,0)$]. After placing the phantom, the system

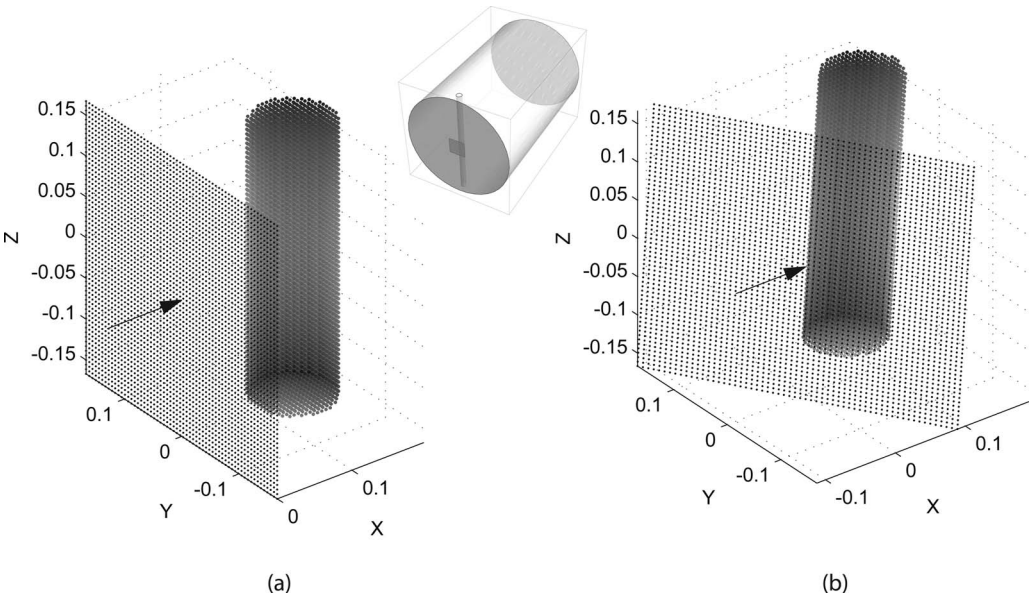

Fig. 3 The central inset is a drawing of the solid phantom (1 cm diameter × 3 cm length) showing a 1-mm-dim drilled hollow column filled with fluorochrome. The boxed area corresponds to the excitation/acquisition window used. (a) The interface surface in this configuration is oriented perpendicular to the excitation beam (arrow). (b) The interface surface is oriented at a given angle to the incident excitation beam (arrow). Each point in the plane represents an acquisition point. In the cylinder, the points represent positions of the fluorescence sources used to simulate the emission through the interface surface. Units in (a) and (b) are mm.

was automatically focused by running the focus search mechanism. Figure 4(a), shows the image obtained on the left, together with the excitation spot on the interface surface on the right, which was obtained by removing, after fluorescence acquisition, the filter F and reducing the sensitivity of the PMT by limiting the number of acquired voltage samples per pixel from 0.5 Ms to 0.05 Ms. Note that the system generates an image of the excitation spot extended by its convolution with the scaled detection pinhole on the surface.

In order to compare the fluorescence intensity distribution with that theoretically expected, the acquired data on the surface, $J(\vec{r}_i,\vec{r}_k)$ was transformed to a new data set corresponding to what would be acquired by the same excitation source and detector spatial distribution but in an unbounded medium, $U^{inf}(\vec{r}_i,\vec{r}_{exc})$, using the formula[12]

$$U^{\inf}(\vec{r}_i,\vec{r}_{exc}) = C_{nd}J(\vec{r}_i,\vec{r}_{exc}) + \frac{dA}{4\pi D}\sum_{j=1}^{N}\left[C_{nd}D\frac{\partial g(\kappa|\vec{r}_j-\vec{r}_i|)}{\partial \vec{n}_j} + g(\kappa|\vec{r}_j-\vec{r}_i|)\right]J(\vec{r}_i,\vec{r}_{exc}), \quad (1)$$

where g is the Green function, $g(\alpha)=\exp(i\alpha)/\alpha$, $D=1/3\mu_s'$ and $\kappa=3\mu_a\mu_s'$, where μ_a and μ_s' are the absorption and reduced scattering coefficients, respectively, and dA is the projection of the sensor aperture onto the surface (assumed to be a constant plane with parameters obtained by fitting the registered surface data). In Eq. (1), we use the refractive index mismatch, C_{nd}, as 5.

Figure 4(b) shows a window of 30 × 30 centered pixels resulting from the calculation specified by Eq. (1) and carried out using the complete 60 × 60 registered intensity data of Fig. 4(a). This clipped window discards the representation of pixels with inconsistent values caused by the border effect inherent in the squared truncation of the data due to the limited sampling area. Figure 4(d) on the left shows the fluorescence intensity distribution for the excitation spot on the surface shown on the right $[\vec{r}_{exc}=(0,-0.05,0)]$. Panel (e) in Fig. 4 shows the result of Eq. (1) applied to the fluorescence data.

The image in panel (a) of Fig. 4 shows a structure in the form of a notch. This corresponds to similar features in the phantom surface that were observed by inspection using conventional illumination in reflection and was caused by the surface cutting. The emergence of these features in the fluorescence images is not due to absorption but corresponds to deficits in the flux after traversing the surface due to the presence in the light of high spatial frequencies—generated by surface irregularities in the fluorescence light traversing the interface—above the cutoff frequency of the optical acquisition system limited by the numerical aperture (NA) 0.13 of L_7. Although these structures are artifacts in the reconstruction data set, their observation in focus means that the surface is correctly conjugated onto the detector plane.

Another characteristic in the data is the presence of autofluorescence arising in the form of a circular spot centered at the excitation location. This can be more clearly seen in the right image of panel (d) in Fig. 4. Discarding the other components used to fabricate the phantom, the autofluorescence term in the intensity is generated close to the surface by the resin.

In a second experiment, the excitation point $\vec{r}_{exc}=(0,0,0)$ was again used, decreasing the laser power to reduce the autofluorescence component in the signal, whereas the surface was tilted as shown in Fig. 3(b). In this case, the translation stage moves for each position associated to each pixel before acquisition of the fluorescence intensity, encod-

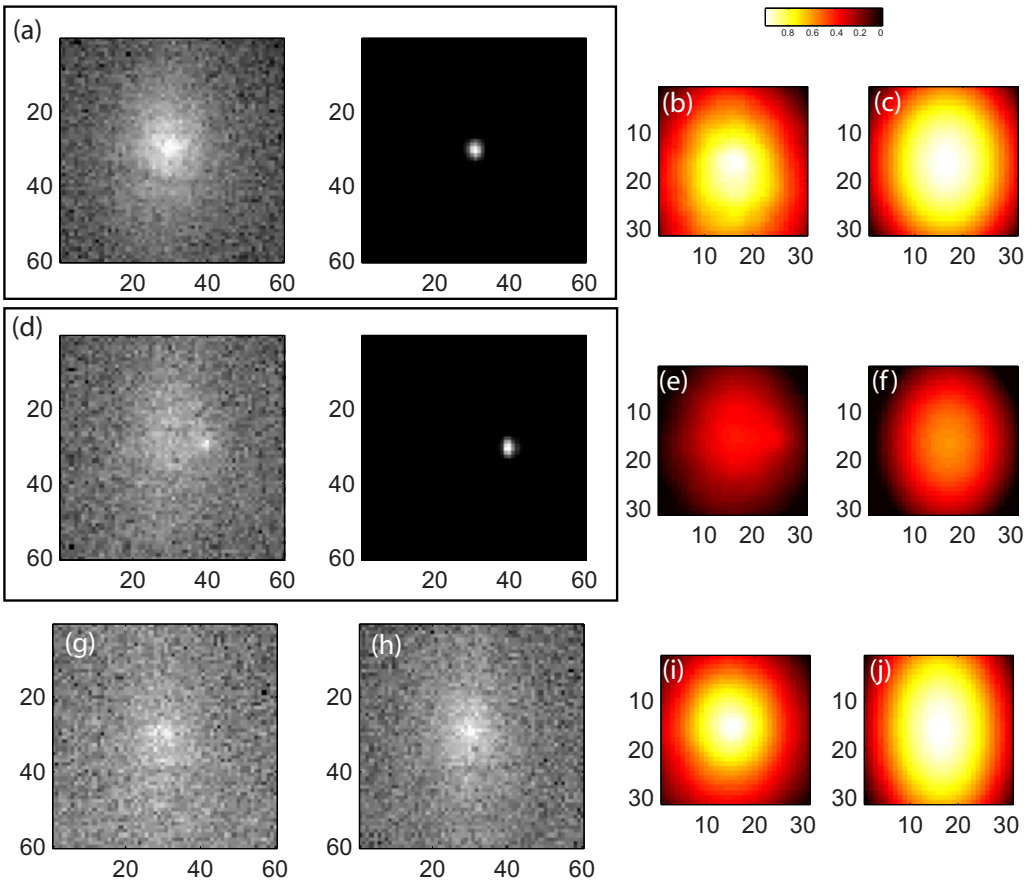

Fig. 4 (a) Fluorescence distribution (in the left panel) for the phantom placed as shown in Fig. 3(a) and the excitation spot (in the right panel); (b) the data transformed using Eq. (1); (c) the corresponding simulated distribution; (d) the fluorescence image (on the left) for a displaced excitation spot (image on the right); (e) the previous data after the use of Eq. (1); (f) the corresponding simulated image; (g) fluorescence image obtained for the phantom placed as shown in Fig. 3(b); (h) the data obtained with the translation stage static; (i) the result of Eq. (1) applied to the data represented in panel (g); (j) the corresponding simulated data.

ing the surface in the process. Figure 3(b) shows the fitted plane obtained from the data. Figure 4(g) shows the intensity distribution obtained, while panel (i) shows the result using Eq. (1).

Figure 4(h) shows the acquired image for this excitation coordinate when, after adjusting the focus for the detector position $\vec{r}=(0,0,0)$, the translation stage remains static during registration at the other transversal detector coordinates. Equation (1) was used and the result compared with the intensity distribution represented in Fig. 4(i). Figure 5 shows the pixel values along a horizontal cut at the center of both images, demonstrating that the first effect of defocusing the surface points (other than those close to the central vertical axis) is a weaker signal.

3.2 *Comparing the Acquired Data with the Numerical Simulation*

In an infinite medium, assuming a uniform discretized fluorochrome distribution $\phi(\vec{r}_j)$ inside a given voxelated volume, V, within a uniform scattering and absorption coefficient limited by a surface S, the average intensity at point $\vec{r}_i$ due to a point static excitation source at $\vec{r}_{exc}$ is given by[13]

$$U(\vec{r}_i,\vec{r}_{exc})=\frac{1}{4\pi D}\sum_{j=1}^{N}\phi(\vec{r}_j)g(\kappa|\vec{r}_j-\vec{r}_{exc}|)g(\kappa|\vec{r}_j-\vec{r}_i|). \quad (2)$$

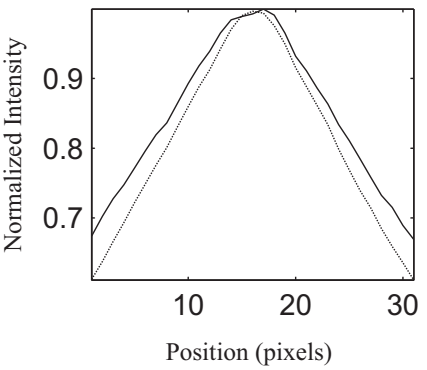

Fig. 5 Comparison between the horizontal normalized intensity profiles versus pixel values when the pinhole is dynamically conjugated with the surface for the different acquisition points (solid line) and when the pinhole remains conjugated only with the central acquisition point (dotted line).

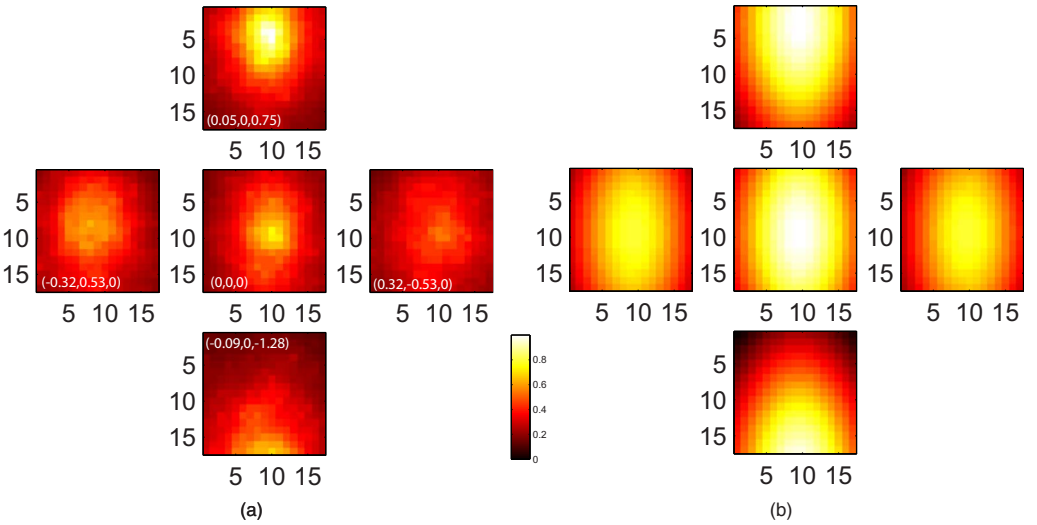

Fig. 6 (a) Fluorescence data of virtual detectors placed in the interface surface for different excitation coordinates of the phantom of Fig. 3(b). (b) Simulated data using Eq. (2). The 15×15 pixels images are normalized using the ensemble maximum and minimum values.

In the phantom, $\phi(\vec{r}_j)$ represent a cylindrical distribution, whose orientation and exact position with respect to the optical axis is approximately known since it is manually placed. Equation (2) allows quantitative comparison of the experimental data—once transformed by Eq. (1)—and the expected intensity distribution.

Figures 4(c) and 4(f) shows the result of the simulation using Eq. (2) when the phantom is placed as in Fig. 3(a) for excitation sources at $\vec{r}_{exc}=(0,0,0)$ and $\vec{r}_{exc}=(0,-0.05,0)$, respectively. Only relatively low intensity values of the image in panel (c) can be compared with pixels of low intensity in (b) since the original data [Fig. 4(a)] contain information of fluorescence together with autofluorescence for the central pixels. Some distortion is caused by the lack of information on the fluorescence intensity caused by the surface notch. The intensity distribution in panel (e) of Fig. 4 is comparable with the simulated intensity distribution of panel (f), after discounting the distortion in the elliptical shape that the autofluorescence peak causes. The image in panel (j) corresponds to the intensity distribution expected for the configuration shown in Fig. 3(b) and excitation at $\vec{r}_{exc}=(0,0,0)$. Again, to discard the autofluorescence, when comparing with the image of panel (i) corresponding to the data obtained from the same phantom position, only pixels distant enough from the image center can be considered, showing the elliptical shape predicted by the simulation.

As a final example, Fig. 6(a) shows a window of 15×15 pixels of the data set computed using Eq. (1) from the 30×30 surface virtual detectors and surface data when the phantom is placed as in Fig. 3(b) using the previous acquisition voltage range and several excitation points. In this case, the pixel size is better matched with the diameter of detection pinhole on the surface. In the horizontal direction, the excitation coordinates for which the data are shown correspond approximately to the system fluorescence signal detection limit. Figure 6(b) shows the simulation results using Eq. (2) for the same excitation points. The reason for these images appearing noisier than the image in Fig. 4(i) is not due to a different excitation intensity but to the use of fewer values in the sum of Eq. (1) and the lower degree of filtering resulting from convolution with the detection pinhole in the registered data. Despite the autofluorescence component in the signal, it can be affirmed that the registered data follow the expected fluorescence intensity distribution.

4 Conclusion

In this paper, we propose a new optical tomography acquisition system. We have shown preliminary results for a high sampling density of light traversing the air/medium surface generated by fluorochrome distribution inside a simulated biological tissue while, simultaneously, determining the interface topography.

The system was constructed to demonstrate the concept by means of the simplest implementation. With the current setup, the main constraint to the number of samples is the acquisition time, which is limited by the focus search algorithm using the confocal principle, which relies on the speed of the motorized translation stage (100 mm/s). This is a simple solution to focus correction, although other optoelectronic devices may offer better performance—for example, those used in adaptive optics.

The use of the confocal principle has the advantage of compactness and eliminates any disparity between the measured intensity and the corresponding interface area. The main cost is a small loss in fluorescence light in the beamsplitter and the difficulties inherent in analyzing intensity variation for different focus. This is, however, not the only possibility, since if co-registration is renounced, other depth resolving techniques could be used to drive the focus correction mechanism.

By changing the optics, our system could easily be modified to increase the field of view and the excitation area and to augment the numerical aperture of the acquisition system. In future realizations, the sensitivity can be improved by choosing the optics to minimize losses and using a new digitizer to

increase the sampling resolution of the sensor output voltage. Furthermore, the excitation optical subsystem could be simplified by omitting the conjugation of the scanner mirrors.

Last, it should be noted that, although the system was applied to optical fluorescence tomography in reflection, the general illumination-acquisition scheme could easily be applied to optical fluorescence tomography in transmission or to other optical tomography modalities in reflection or transillumination.

Acknowledgment

The authors gratefully acknowledge financial support from the Ministerio de Education y Ciencia, Spain (Grant No. FIS2005-01569).

References

1. V. Ntziachristos, J. Ripoll, L. V. Wang, and R. Weissleder, "Looking and listening to light: the evolution of whole-body photonic imaging," *Nat. Biotechnol.* **23**(3), 313–319 (2005).
2. J. Ripoll, R. B. Schulz, and V. Ntziachristos, "Free-space propagation of diffuse light: theory and experiments," *Phys. Rev. Lett.* **91**(10), 103901 (2003).
3. R. B. Schulz, J. Ripoll, and V. Ntziachiristos, "Experimental fluorescence tomography of tissues with noncontact measurements," *IEEE Trans. Med. Imaging* **23**(4), 1–9 (2004).
4. H. Meyer, A. Garofalakis, G. Zacharakis, C. Mamalaki, D. Kioussis, E. N. Economou, V. Ntziachristos, and J. Ripoll, "Non-contact optical imaging in mice with full angular coverage and automatic surface extraction," *Appl. Opt.* **46**, 3617–3627 (2007).
5. J. Ripoll and V. Ntziachristos, "Imaging scattering media from a distance: theory and applications of non-contact optical tomography," *Mod. Phys. Lett. B* **18**(28–29), 1403–1431 (2004).
6. Z.-M. Wang, G. Y. Panasyuk, V. A. Markel, and J. C. Schotland, "Experimental demonstration of an analytic method for image reconstruction in optical diffusion tomography with large data sets," *Opt. Lett.* **30**(24), 3338–3340 (2005).
7. A. Joshi, W. Bangerth, and E. M. Sevick-Muraca, "Non-contact fluorescence optical tomography with scanning patterned illumination," *Opt. Express* **14**(14), 6516–6534 (2006).
8. N. Deliolanis, T. Lasser, D. Hyde, A. Soubret, J. Ripoll, and V. Ntziachristos, "Free-space fluorescence molecular tomography utilizing 360 degree geometry projections," *Opt. Lett.* **32**(4), 382–384 (2007).
9. D. Kepshire, S. C. Davis, H. Dehghani, K. D. Paulsen, and B. W. Pogue, "Fluorescence tomography characterization for subsurface imaging with protoporphyrin IX," *Opt. Express* **16**(12), 8581–8593 (2008).
10. T. Wilson, Ed., *Confocal Microscopy*, Academic Press, London (1990).
11. R. Cubeddu, A. Pifferi, P. Taroni, A. Torricelli, and G. Valentini, "Solid tissue phantom for photon migration studies," *Prog. Met. Phys.* **42**, 1971–1979 (1997).
12. J. Ripoll and V. Ntziachristos, "From finite to infinite volumes: removal of boundaries in diffuse wave imaging," *Phys. Rev. Lett.* **96**, 173903 (2006).
13. V. Ntziachristos and R. Weissleder, "Experimental three-dimensional fluorescence reconstruction of diffuse media by use of a normalized Born approximation," *Opt. Lett.* **26**(12), 893–895 (2001).